This document is the Accepted Manuscript version of a Published Work that appeared in final form in ACS Nano, copyright © 2024 American Chemical Society after peer review and technical editing by the publisher. To access the final edited and published work see https://doi.org/10.1021/acsnano.4c07907.

Missing-linker Defect Functionalized Metal-organic Frameworks Accelerating Zinc Ion Conduction for Ultrastable All-Solid-State Zinc Metal Batteries

Xiaobin Hui, Zhen Zhan, Zeyu Zhang, Jingya Yu, Pengyan Jiang, Zhengzheng Dang, Jian Wang, Songhua Cai,* Yanming Wang,* Zheng-Long Xu*

X. Hui, J. Yu, P. Jiang, Z.L. Xu

State Key Laboratory of Ultra-precision Machining Technology, Research Institute for Advanced Manufacturing, Department of Industrial and Systems Engineering, The Hong Kong Polytechnic University, Hung Hom, Hong Kong SAR, China

Email: <u>zhenglong.xu@polyu.edu.hk</u> (ZL Xu)

Z. Zhan, S. Cai

Department of Applied Physics, The Hong Kong Polytechnic University, Hung Hom, Hong Kong SAR, China

Email: songhua.cai@polyu.edu.hk (S Cai)

Z. Zhang, Z. Dang, Y. Wang

University of Michigan-Shanghai Jiao Tong University Joint Institute, Shanghai Jiao Tong University, Shanghai 200240, China

Email: yanming.wang@sjtu.edu.cn (Y Wang)

J. Wang

School of Energy and Environment, City University of Hong Kong, Hong Kong SAR, China.

Abstract

Solid-state polymer electrolytes (SPEs) are promising for high-performance zinc metal batteries (ZMBs), but they encounter critical challenges of low ionic conductivity, limited Zn^{2+} transference number (tz_{n}^{2+}), and unstable electrolyte-electrode interface. Here, we present an effective approach involving a missing-linker metallic organic framework (MOF)-catalyzed poly (ethylene glycol) diacrylate (PEGDA)/polyacrylamide (PAM) copolymer SPE for single Zn^{2+} conduction and seamless electrolyte-electrode contact. The single- Zn^{2+} conduction is facilitated by the anchoring of OTF- anions onto the unsaturated metal sites of missing-linker MOF, while the PEGDA and PAM chains in competitive coordination with Zn^{2+} ions promote rapid Zn ion transport. Our all-solid-state electrolyte simultaneously achieves a superior ionic conductivity of 1.52 mS cm⁻¹ and a high tz_{n}^{2+} of 0.83 at room temperature, alongside uniform Zn metal deposition (1000 cycles in symmetric cells) and high Zn plating/striping efficiencies (>99% after 600 cycles in asymmetric cells). Applications of our SPE in Zn//VO2 full cells are further demonstrated with a long lifespan of 2000 cycles and an extremely low-capacity degradation rate of 0.012% per cycle. The strategies of using missing-linker MOF to catalyze competitively coordinating copolymers for accelerating Zn^{2+} ion conduction pave a viable way for developing all-solid-state Zn

Keywords: Zn-ion battery, solid-state electrolyte, defected MOF, single-ion conducting, competitive coordination.

Aqueous zinc metal batteries (ZMBs) have been recognized promising for the next generation energy storage systems due to the high theoretical capacity (820 mAh g⁻¹) and low redox potential (0.76 V vs. standard hydrogen electrode) of Zn metal, and the low-cost, non-toxicity, and high-safety of aqueous electrolytes.^{1, 2} Nevertheless, the practical implementation of aqueous ZMBs is hindered by the concomitant problems of dendrite growth, surface passivation, and corrosion from hydrogen evolution reaction, all of which are exacerbated by the aqueous electrolytes.^{3, 4} Solid-state polymer electrolytes (SPEs) emerge as a viable solution to these issues by offering superior safety and stability due to their liquid-free nature.^{5, 6} The kinetics of ionic transfer for solid-state electrolytes plays a significant role in determining the electrochemical performance of ZMBs, especially for the cycling stability and rate capability.

An ideal solid-state electrolyte for advanced ZMBs should possess several critical attributes: i) a high Zn²⁺ ionic conductivity (>10⁻³ S cm⁻¹) to facilitate rapid ion transport and enhance electrochemical reaction kinetics, ii) a selective Zn²⁺ transfer with high Zn²⁺ ion transference numbers (t_{zn2+}) to minimize anionic accumulation and cell polarization, iii) a stable electrolyte-electrode interface that ensures fast and uniform Zn²⁺ ion transport.⁷ Regrettably, the current SPEs fall short in meeting these requirements. These SPEs, composed primarily of zinc salts and a polymer matrix which deliver Zn²⁺ ion diffusion *via* a hopping mechanism that occurs in tandem with the random movement of polymer chains, show poor ionic conductivities (10⁻⁷ to 10⁻⁵ S cm⁻¹).⁸ Moreover, they typically function as binary-ion conductors that allow the concurrent movement of Zn²⁺ ions and the counter anions, which results in low Zn²⁺ transference numbers (t_{Zn2+} < 0.4).^{9, 10} According to the classical Sand's time equation, a low t_{Zn2+} (or high anion transference number) renders the earlier Zn metal dendrite nucleation, while the accumulation of anions on the anode surface causes serious side reactions and cell polarization. These obstacles collectively retard the advancement of solid-state ZMBs.^{11, 12}

An effective approach to address these issues is constructing single-ion conductors (SICs), in which anions or negative-charged small molecules are covalently bonded to polymeric or inorganic backbones to create Lewis basic sites for selective cationic transport.^{11, 13} However, achieving high t_{Zn2+} in previous Zn^{2+} SICs often compromised the Zn^{2+} conductivity. For example, a polymeric SIC with heterocyclic tetrazole anionic centers on its side chains delivered a t_{Zn2+} of 0.94, close to unity, but exhibiting a low Zn^{2+} ionic conductivity of 0.54 mS cm⁻¹, around one-quarter of commercial glass fiber separators in liquid electrolytes.^{14, 15} The poor ionic conductivity can be attributed to the limited Zn^{2+} concentration in the SICs synthesized by ionic exchange methods, and the restricted Zn^{2+} diffusion due to the strong interactions between Zn^{2+} and anionic sites. Furthermore, the complex fabrication procedures of current Zn^{2+} SICs, including grafting, polymerization, and cation replacement, followed by their *ex-situ* insertion between electrodes, induce significant manufacturing costs and high interfacial resistance.¹⁶⁻¹⁸ Consequently, developing Zn^{2+} SICs with high ionic conductivity, high $t_{Zn^{2+}}$, and seamless electrode-electrolyte interface remains a formidable challenge.

In this work, we regulate the anionic and cationic motions simultaneously in SPEs by introducing a missing-linker metal organic framework (MOF) to anchor anions in dissociated zinc salt and to catalyze the formation of copolymer matrix with low-energy Zn²⁺ diffusion pathways for accelerated Zn²⁺ conduction in high-performance ZMBs. Specifically, we designed a carboxyferrocene (Fc) modulated missing-linker MOF (designated as MOF-Fc) with open Co²⁺ sites to bond OTF⁻ through strong Lewis acid-base interactions to accelerate the dissociation of Zn(OTF)₂ salt and anchor OTF⁻ anions for single-Zn²⁺ conduction. The MOF-Fc is then introduced to minimize the crystallinity of polyacrylamide (PAM) and poly(ethylene glycol) diacrylate (PEGDA) copolymer matrix (denoted as PM), thereby enhancing the mobility of local polymer chains and the coordinated Zn²⁺ ions. The ether oxygen groups (-O-) in PEGDA and the amide groups (NH₂-C=O) in PAM show competitive coordination toward Zn²⁺ ions, which significantly reduces the Zn²⁺ desolvation energies for transport. Profiting from the synergistic interplay between the anion-anchoring capability of MOF-Fc and the Zn²⁺ transport property in PM matrix, the resulting all-solid-state electrolyte (denoted as MOF-Fc@PM) simultaneously achieves an exceptional ionic conductivity of 1.52 mS cm⁻¹ and a *tz*n₂₊ of

0.83 at room temperature, rivaling the state-of-the-art SPEs in ZMBs. Applications of the *in-situ* polymerized electrolytes directly onto electrode surfaces create an integrated electrolyte-electrode interface with outstanding compatibility and stability, enabling 1000 cycles of dendrite-free Zn plating/stripping and ultrastable Zn//VO₂ full cells for 2000 cycles. This study offers a promising solution for the design of accelerated single-Zn²⁺ ion conduction in SPEs for all-solid-state Zn batteries.

Results and Discussion

Fabrication and properties of missing-linker MOF

As shown in **Figure 1**, the synthesis of MOF-Fc@PM electrolyte encompasses two primary steps, namely, the construction of missing-linker MOF and the co-polymerization of PEGDA and PAM with MOF. Firstly, the Fc is incorporated into MOF to partially substitute the 2-aminoterephthalic acid (TPA-NH₂) ligands, resulting in a MOF-Fc enriched with open Co²⁺ sites. ^{19,20} Then, the missing-linker MOF is functionalized with methacryloyl groups, which serve as important grafting points for the following co-polymerization process. The final step involves the one-pot solidification of a homogeneous mixture containing MOF-Fc, PEGDA+AM monomers, Zn(OTF)₂ salt, and a thermal initiator *via* a radical polymerization method to yield the solid-state MOF-Fc@PM films. The MOF-Fc is pivotal in determining the properties of MOF-Fc@PM, thus necessitating comprehensive characterizations.

Pristine MOF shows a nanosheet morphology of 2 to 5 μm in size (**Figure S1**). After incorporating with Fc missing linkers, the MOF-Fc retains its original morphology and displays an evenly distributed Fe signal in the elemental mapping (**Figure S2**), suggesting the successful introduction of Fc into the MOF structure. The density functional theory (DFT) calculated structural models of MOF and MOF-Fc in **Figure S3** confirm the thermodynamic viability of replacing TPA-NH₂ ligands with Fc. Inductively coupled plasma mass spectrometry (ICP-MS) quantifies the Fc ligands content at 20.71% in MOF-Fc (**Table S1**).

To pinpoint the defects in the missing-linker MOF, we conducted the low-dose integrated differential phase contrast-scanning transmission electron microscopy (iDPC-STEM), a technique that facilitates the visibility of light elements such as carbon (C) and oxygen (O). $^{21-24}$ Figure 2a and b depict the iDPC-STEM images of pristine MOF, in which the Co-O layers interspaced by TPA-NH₂ ligands are clearly discerned without visible defects. The lattice spacing of 9.5 Å between Co layers corresponds to the (001) plane, aligning with the DFT-modeled structures (Figure 2c). In contrast, noticeable missing-linker defects are observed for MOF-Fc (marked with orange circles in Figure 2d, e). These defects are characterized by the bonding of Fc ligands to Co atoms *via* the carboxyl ends, concurrently generating unsaturated Co sites on the opposite side (Figure 2f). In the defective region, the Co layers for MOF-Fc show a (001) lattice space of 9.2 Å, the slight deviation may be attributed to the lattice strain induced by missing linker defects. Figure 2g-j and Figure S4 depict the strain mapping by geometric phase analysis (GPA) for MOF and MOF-Fc. Obviously improved variations in the strain distribution, especially in the E_{yy} direction (normal strain in a direction close to parallel with 2D layers), are observed for MOF-Fc in comparison to the pristine MOF. The pronounced strain for MOF-Fc indicated the integration of Fc into MOF and the increased open Co²⁺ sites and lattice distortions. ²⁵

To elucidate the influence of Fc missing linkers on the electronic state and coordination structure of MOF, we performed X-ray photoelectron spectroscopy (XPS) and electron paramagnetic resonance (EPR) characterizations. After Fc incorporation, a discernible Fe 2p peak is detected in the general XPS spectrum of MOF-Fc (**Figure S5**). The deconvoluted Co 2p and O 1s XPS spectra exhibit a noticeable red-shift relative to pristine MOF (Figure S5b and c), suggesting changes in the Co coordination environment by Fc missing linkers. Furthermore, the MOF-Fc exhibits a valence band maximum energy of 0.87 eV (Figure S5d), which is 0.45 eV lower than that of pristine MOF, confirming the modulatory effect of Fc on the electronic structure of MOF. The EPR curve of MOF-Fc reveals a pronounced signal peak at g = 2.004 with enhanced intensity and breadth in comparison to pristine MOF (**Figure S6a**). This observation highlights the increased presence of unpaired electrons

and unsaturated Co²⁺ sites in MOF-Fc.²⁰

The Co K-edge X-ray absorption near-edge structure (XANES) spectra of MOF and MOF-Fc resemble that of CoO (Figure S6b), suggesting a Co²⁺ valence state in the MOF samples. However, the MOF-Fc spectrum shows reduced peak intensity from the lower coordination number of Co centers. The extended X-ray absorption fine structure (EXAFS) oscillations of MOF-Fc in Figure S6c exhibit a smaller amplitude than MOF, once again suggesting a reduced average coordination number (CN) of Co sites. ^{19, 20} Fourier transform analysis of the EXAFS spectra for both MOF and MOF-Fc reveals a primary peak at around 1.5 Å (Figure S6d), corresponding to the Co-O bond length. Notably, MOF-Fc displays a lower Co-O CN (4.20 \pm 0.84) than the pristine MOF (6.54 \pm 0.87) (Figure S6e and **Table S2**), ²⁷ which provides direct evidence for the successful incorporation of Fc into MOF. These comprehensive characterizations elucidate the introduction of a wealth of unsaturated Co sites by Fc in MOF structure, which will play a pivotal role as anion anchors in the MOF-Fc@PM electrolyte.

Properties of missing linker MOF-regulated MOF-Fc@PM electrolyte

The missing-linker MOF are firstly modified by methacryloyl chloride to construct polymer grafting points on the surface. As shown in the Fourier transform infrared (FTIR) spectra (**Figure S7**), after the methacryloyl chloride modification, the characteristic peak at 3306 cm⁻¹ corresponding to -NH₂ groups of MOF(-Fc) disappears, but the peak at 3145 cm⁻¹ for O=C-NH remains. A new peak at 1640 cm⁻¹ referring to C=C appears for the modified MOF samples. These results collectively confirm the replacement of -NH₂ by methacryloyl groups. Then, the modified missing-linker MOF is employed to catalyze the copolymerization of PEGDA and PAM into MOF-Fc@PM electrolyte. As shown in **Figure S8** and **Figure S9**, both MOF@PM and MOF-Fc@PM exhibit the compact structure for interconnected ion transport network. Energy-dispersive X-ray spectra (EDS) mappings show the homogeneous dispersion of C, O (mainly from polymer matrix), Zn, F (from Zn(OTF)₂ salts), Co, Fe (from MOF or MOF-Fc) elements, which confirms the uniform distribution of zinc salts and MOF fillers in the composite electrolytes.

To evaluate the influence of MOF-Fc on the microstructure of SPEs, X-ray diffraction (XRD) and differential scanning calorimetry (DSC) measurements were performed. As illustrated in Figure 3a, the PM copolymer exhibits a semi-crystalline structure with a broad peak at approximately 20°. The introduction of MOF fillers results in significantly reduced peak intensities for MOF@PM and MOF-Fc@PM, suggesting the disrupted crystalline domain from the crosslinking of MOFs with polymers.²⁸ We also observed a notable decrease in the glass transportation temperature (T_g) of PM from -46 °C to -57 °C for MOF-Fc@PM (Figure 3b). According to Vogel-Tamman-Fulcher theory,²⁹ the amorphous microstructure and reduced $T_{\rm g}$ of MOF-Fc@PM are conducive to polymer chain movement and the association/disassociation of Zn²⁺ ions. Thermogravimetric analysis (TGA, Figure S10a) indicated the enhanced thermal stability of MOF-Fc@PM over PM, which can be attributed to the full crosslinking of polymer chains and the structure reinforcement by MOF-Fc. The tensile stress-strain curves of PEGDA, PM, MOF@PM, and MOF-Fc@PM electrolytes were also conducted (Figure S10b). Unlike the mechanically weak PEGDA electrolyte, the PM copolymer electrolyte exhibits considerable improvements in the tensile strength (1.68 MPa) and elongation at-break (20.5%) due to the increased crosslinking degree. The incorporation of MOF-Fc further augmented the tensile strength up to 4.9 MPa and the elongation-at-break value to 35.5% for MOF-Fc@PM, demonstrating improved mechanical robustness of the SPE.

The interactions between MOF-Fc and copolymer matrix were examined by FTIR and Raman spectroscopy. Characteristic FTIR peaks at 3306 cm⁻¹ and 3145 cm⁻¹, attributed to -NH₂ groups on the surface of MOF and MOF-Fc fillers, are evident in Figure 3c.³⁰ MOF@PM and MOF-Fc@PM display no FTIR peaks at 1617 cm⁻¹ for the C=C bond, confirming the complete polymerization of PEGDA and AM monomers.³¹ New characteristic FTIR peaks at 1445 cm⁻¹, 1727 cm⁻¹, and 2891 cm⁻¹, corresponding to the amide group on PAM, carboxyl groups on PEGDA, and alkyl on polymer chains, are observed. FTIR results confirm that PM copolymers are fully crosslinked and successfully grafted on the surface of MOF-Fc. Moreover, the bending vibration of Zn-O bond in Zn(OTF)₂ salts at 645

cm⁻¹ shifts to lower wavenumbers in the PM, MOF@PM, and MOF-Fc@PM electrolytes, indicative of Zn(OTF)₂ dissociation among polymer chains (Figure 3d).³² A detailed comparison reveals the most pronounced shift to 632 cm⁻¹ for MOF-Fc@PM, suggesting the highest Zn(OTF)₂ dissociation degree. It is further corroborated by the substantial FTIR peak shift of S=O/S-O vibrations for OTF⁻ anions from 1037 cm⁻¹ in Zn(OTF)₂ salt to 1020 cm⁻¹ in MOF-Fc@PM (Figure 3d).^{33,34} Raman result supports these findings by showing noticeable redshifts for the C-F and S=O/S-O vibrations for OTF⁻ anions in Zn(OTF)₂ and MOF-Fc@PM (Figure 3e and f).^{35,36} These spectroscopic analyses suggest that MOF-Fc effectively promotes the dissociation of Zn(OTF)₂ salt and immobilizes OTF⁻ anions, thereby enhancing Zn²⁺ conduction in SPEs.

To substantiate the effectiveness of MOF-Fc in anchoring OTF⁻ anions, Co K-edge XANES analysis was conducted on MOFs immersed in $Zn(OTF)_2$ aqueous solution with the samples designated as MOF-OTF⁻ and MOF-Fc-OTF⁻. As shown in Figure 3g and Figure S10c, MOF-Fc-OTF⁻ exhibits a Co K-edge energy shift of +0.74 eV to MOF-Fc, indicative of strong host-guest interactions between the open Co^{2+} sites and OTF⁻ anions.³⁷ Conversely, the pristine MOF in $Zn(OTF)_2$ solution shows a negligible Co K-edge shift. Moreover, analysis of the fitted EXAFS spectra (Figure 3 h, i and Table S2) reveals an increase in the Co-O CN from 4.20 for MOF-Fc to 6.86 for MOF-Fc-OTF⁻, resulting in a greater Δ CN = 2.66 than the Δ CN = 0.37 for pristine MOF. These results validate the coordination between open Co^{2+} sites in MOF-Fc and OTF⁻ anions.

The Zn²⁺ coordination environment among PM chains was probed by ⁶⁷Zn nuclear magnetic resonance (NMR) spectroscopy of Zn(OTF)₂ solutions containing PEGDA, PAM or PM polymers. The introduction of PEGDA or PAM into the Zn(OTF)₂ solution resulted in a notable increase in the ⁶⁷Zn chemical shift and the peak half-width (Figure 3j) due to the strong coordination of Zn²⁺ ions by the oxygenated segments in the polymers. The largest ⁶⁷Zn chemical shift (0.14 ppm) for Zn(OTF)₂/PAM suggests the strongest coordination strength of PAM towards Zn²⁺ *via* the hydrophilic NH₂-C=O groups.³⁸⁻⁴⁰ Interestingly, the ⁶⁷Zn chemical shift for Zn(OTF)₂/PM reverted to -2.29 ppm,

comparable to that of Zn^{2+} - H_2O in $Zn(OTF)_2$ aqueous solution. This result suggests the competitive coordination of PEGDA and PAM polymer chains with Zn^{2+} , possibly forming a Zn^{2+} migration channel with low desolvation energies, which will be further elucidated in our theoretical calculations.

Ionic transfer kinetics of the anhydrous MOF-Fc@PM electrolyte were investigated at room temperature in comparison with PEGDA, PM, and MOF@PM electrolytes. As shown in **Figure 4**a, the ionic conductivity of MOF-Fc@PM reached 1.52×10^{-3} S cm⁻¹, significantly surpassing the 0.36×10^{-4} S cm⁻¹ for PEGDA electrolyte, 1.07×10^{-4} S cm⁻¹ for PM electrolyte, and 9.21×10^{-4} S cm⁻¹ for MOF@PM electrolyte. The superior ionic conduction for MOF-Fc@PM is evidenced by the lowest activation energy (E_a) of 33.0 kJ mol⁻¹ among these four electrolytes (Figure 4b). Furthermore, the tz_{n2+} of these SPEs was determined using a Bruce-Vincent method with values following the descending order of MOF-Fc@PM ($tz_{n2+} = 0.83$) > MOF@PM ($tz_{n2+} = 0.68$) > PM ($tz_{n2+} = 0.29$) > PEGDA ($tz_{n2+} = 0.21$) (Figure 4c and **Figure S11**). The high tz_{n2+} of MOF-Fc@PM provides a testament to the immobilization OTF⁻ anions by MOF-Fc as discussed earlier. It should be noted that negligible difference is observed for the tz_{n2+} between PM and PEGDA, which may be attributed to the intrinsic binary-ion conducting feature for pure polymer electrolytes. Besides, the pore sizes of MOF and MOF-Fc are much larger than the dimensions of OTF⁻ anions (3.05 Å) and Zn²⁺ cations (1.48 Å) (**Figure S12**), which neglects the influence of pore structures on the ionic diffusion kinetics.

DFT calculations for the Zn ion transfer mechanism

To gain more insights into the working mechanism of MOF-Fc@PM electrolyte, we conducted DFT calculations to study the anchoring effect of MOF-Fc to OTF⁻ and the competitive coordination of PM copolymer to Zn²⁺ ions. Firstly, we compared the configurations and binding energies of OTF⁻ or Zn²⁺ absorbing onto MOF and MOF-Fc (Figure 4d-f). The MOF demonstrates an adsorption energy of -1.81 eV to OTF⁻ anion. The adsorption configuration reveals a Co-O/OTF⁻ distance of 3.63 Å and the formation of a hydrogen bond between the OTF⁻ O atoms and the hydroxyl group from MOF. It suggests that the adsorption is likely influenced by both van der Waals interactions and hydrogen

bonding. In sharp contrast, the open Co²⁺ sites of MOF-Fc displayed a higher OTF⁻ adsorption energy of -2.57 eV and a substantially reduced Co-O/OTF⁻ distance of 1.54 Å. The charge-density difference plots (Figure 4e) depict the pronounced electron transfer from the unsaturated Co²⁺ sites on MOF-Fc to the OTF⁻ oxygen atom, demonstrating the strong adsorption effect of MOF-Fc toward OTF⁻ anions. In contrast, MOF-Fc presented a lower Zn²⁺ adsorption energy of -0.25 eV than the -1.14 eV for MOF (Figure 4f and **Figure S13**) due to the electrostatic repulsion between Co²⁺ and Zn²⁺, which favors Zn²⁺ ion transport.

Figure 4g depicts the calculated two-step dissociation energies of Zn(OTF)₂ salt and the solvation energies of Zn²⁺ with PEGDA, PAM, and PM polymer chains. The polymerization degrees of PEGDA and PAM models were set as 3 to balance the computational feasibility and the realistic molecular sizes. For simulating our all-solid-state electrolyte, solvents were omitted from the calculation of Zn²⁺-polymer coordination energies. PAM displayed a Zn²⁺ solvation energy of -15.11 eV, higher than the 1st-step Zn(OTF)₂ dissociation energy of 8.39 eV but lower than the Zn²⁺-PEGDA solvation energy of -16.55 eV. This indicates that Zn(OTF)₂ dissociated more readily in PEGDA, while the moderate Zn²⁺ solvation energy in PAM is conducive for Zn²⁺ diffusion. The PM copolymer resolves this conundrum by presenting a Zn²⁺ solvation energy of -15.62 eV, intermediate between the Zn-OTF⁻ dissociation energy and the Zn²⁺-PEGDA desolvation energy. Therefore, a balance of high Zn(OTF)₂ dissociation degrees and low Zn²⁺ migration barriers was achieved for MOF-Fc@PM. The DFT result in Figure 4g appears to diverge from the ⁶⁷Zn NMR analysis in Figure 3g, which suggested stronger Zn²⁺-PAM interactions. The discrepancy can be ascribed to the influence of H₂O molecules in the ⁶⁷Zn NMR test. Both DFT calculations and ⁶⁷Zn NMR measurements agree on the competitive coordination of Zn²⁺ ions between PEGDA and PAM polymer chains.

Overall, the Zn²⁺ ion conduction mechanism of MOF-Fc@PM can be summarized as follows: the strong Lewis acid-base interaction between MOF-Fc and OTF⁻ anions, coupled with the solvation effect of PM toward Zn²⁺, promotes the dissociation of Zn(OTF)₂ salts. The dissociated OTF⁻ anions

are anchored on the open Co²⁺ sites of MOF-Fc for single Zn²⁺ ion conduction. Concurrently, the competitive coordination from PEGDA and PAM chains establishes a fast Zn²⁺ diffusion channel characterized by low migration barriers. Profiting from the synergistic effect of these astute structures, MOF-Fc@PM presented superior ionic conductivity to its peers (**Table S3**). This renders MOF-Fc@PM a highly promising candidate for high-power and long-lasting ZMBs.

Electrochemical performance of Zn anodes with MOF-Fc@PM electrolyte

To investigate the electrochemical stability of Zn metal anodes in MOF-Fc@PM electrolyte, we assembled Zn//Cu asymmetric cells and Zn//Zn symmetric cells for cycling tests, in comparison with MOF@PM and PM electrolytes. The electrochemical stability window (ESW) was firstly determined by cyclic voltammetry (CV) test at a scan rate of 5 mV s⁻¹. **Figure 5**a shows decent ESWs of above 2.0 V for MOF-Fc@PM and MOF@PM, which is superior to the 1.86 V for PM electrolyte and the 1.2-1.6 V for typical aqueous electrolytes. ^{41, 42} The enhanced ESW can be attributed to the sufficient cross linking between MOF(-Fc) fillers and PM co-polymer matrix. The enhanced interactions between fillers and PM matrix can construct fast Zn²⁺ transfer channels, thus restraining the anion concentration polarization and decomposition at high voltages. ^{31, 43-46} The high oxidation stability makes the composite electrolyte compatible with high-voltage cathodes such as V₂O₅, MnO₂, and VO₂ for Zn metal full cells. ⁴⁷⁻⁴⁹

Coulombic efficiencies (CEs) of Zn//Cu cells were examined at a current density of 1 mA cm⁻² and a cut-off capacity of 1 mAh cm⁻² after the initial two cycles at 2 mA cm⁻² and 2 mAh cm⁻² for electrochemical activation (Figure 5b). It should be noted that most Zn//Cu plating/stripping experiments were performed in liquid or quasi-solid-sate electrolytes in literature, ^{50,51} with the CEs of all-solid-state Zn//Cu cells rarely being reported. The Zn//Cu cells with MOF-Fc@PM electrolyte demonstrated excellent stability, enduring up to 600 cycles (average CE = 99.65%) with much lower overpotentials of 48 mV (Figure 5c and **Figure S14**). This performance is in stark contrast to the PM electrolyte (average CE = 86.31% and failed after 99 cycles) and the unstable CEs for MOF@PM

electrolyte. The low overpotential and ultrastable Zn metal plating/stripping cycles attest to the efficient Zn²⁺ transport of MOF-Fc@PM electrolyte.

Further demonstration of the stability of Zn metal plating and stripping in the MOF-Fc@PM electrolyte was achieved by cycling the Zn//Zn symmetric cells at a current density of 1 mA cm⁻² with a capacity of 0.5 mAh cm⁻² for 1000 cycles. The Zn/MOF-Fc@PM/Zn cells show extremely stable Zn plating/stripping curves with average overpotentials of 0.22 V (Figure 5d), devoid of any voltage oscillation or increase. In contrast, the Zn//Zn cells with PM electrolyte began with a large overpotential of 0.58 V, which dramatically increased until cell failure at the 271th cycle. Although the MOF@PM electrolyte extended the Zn//Zn cycle life to 672 h, they still suffered from progressively increasing overpotentials.

Electrode-electrolyte interface is a critical factor for the cycling stability, overpotential, and CEs of all-solid-state batteries. In general, SPEs are synthesized as free-standing films before insertion between anodes and cathodes. This approach often results in large interfacial resistance from poor solid-solid contact. To address this, we developed an *in-situ* polymerization process by directly polymerizing the MOF-Fc@PM precursors on the electrode surface. As illustrated in **Figure S15**, this method yielded an integrated electrode-electrolyte contact. The *in-situ* polymerized Zn//MOF-Fc@PM//Zn cells can further decrease the overpotential to 0.12 V at a current density of 1 mA cm⁻² over 1000 cycles (Figure 5e). The superior interfacial kinetics afforded by *in-situ* polymerized MOF-Fc@PM were also confirmed by electrochemical impedance spectrum (EIS) measurement. As shown in Figure 5f, the interfacial charge transfer resistance (Ret) for the *in-situ* integrated cell is 242.6 Ω, which is approximately one-third that of the *ex-situ* assembled Zn//Zn cells, indicating the significantly improved interfacial charge transfer kinetics for the *in-situ* cells.

An in-situ-integrated all-solid-state Zn metal battery

Finally, to estimate the practical application potential of the MOF-Fc@PM electrolyte in Zn metal batteries, we assembled all-solid-state Zn//VO₂ cells with Zn foil anodes and VO₂ cathodes, utilizing

either *in-situ* or *ex-situ* polymerized MOF-Fc@PM electrolytes (designated as *in-situ* or *ex-situ* cells, respectively). The morphology and chemical structures of VO₂ cathode materials in this work are comprehensively characterized and displayed in **Figure S16** and **Figure S17**, which indicated nanorod shapes with high purity and crystallinity. The CV curves of the *in-situ* cells show higher peak currents and smaller redox polarizations than the *ex-situ* counterparts (**Figure 6a**), indicating the higher capacity utilization and superior electrochemical reaction kinetics. When galvanostatically cycling at a low current density of 0.1 A g⁻¹ (**Figure S18**), the *in-situ* cells show an initial reversible capacity of 235.3 mAh g⁻¹ with a higher initial CE of 96.1% and lower overpotential of 0.2 V compared to the *ex-situ* cell (85.4% and 0.29 V). The *in-situ* cells retained a capacity of 233.6 mAh g⁻¹ after 100 cycles (Figure 6b), rendering an extremely high capacity retention of 99.2%. Conversely, only 64.1% of the initial capacity was preserved for the *ex-situ* cells. When the current density was increased to 0.5, 1, 3, and 5 A g⁻¹, the discharge capacities for the *in-situ* cells are 190.2, 165.5, 120.8, and 89.3 mAh g⁻¹, respectively, which are much higher than these for *ex-situ* cells (Figure 6c). The poor cycling stability and rate capability for the *ex-situ* cell are likely due to the poor interfacial contact associated with high interfacial impedance and Zn dendrite growth.

The capability of MOF-Fc@PM electrolyte for long-term Zn metal battery was measured by subjecting the *in-situ* cells to 2000 cycles at a high current density of 1 A g⁻¹. They exhibit reversible capacities of 165.8 mAh g⁻¹ at the 1st cycle and 123.9 mAh g⁻¹ at the 2000th cycle, rendering an extremely low-capacity fading rate of 0.012 % per cycle (Figure 6d). Apart from the excellent attributes of the MOF-Fc@PM electrolyte, the *in-situ* polymerization method for fabricating all-solid-state ZMBs with integrated interface is also important. As evidenced by the cross-sectional SEM images (Figure 6e) and EDS mapping (Figure S19), the *in-situ* cell maintains a void-free, well-contacted interface after cycling, demonstrating excellent interfacial stability. Additionally, the cycled Zn anode exhibits a smooth, dendrite-free surface, indicative of a homogeneous and stable Zn plating/stripping process. Conversely, the *ex-situ* cell displays poor interfacial stability with noticeable gaps, resulting

in nonuniform Zn deposition and dendrite formation. In addition, the EIS test for the *in-situ* and *ex-situ* Zn//VO₂ cells before cycling (**Figure S20**) shows that the *in situ* full cell exhibits the lower interfacial R_{ct} of 147.8 Ω than that of ex situ cell (326.1 Ω). Since the solid electrolytes used in *in situ* and ex situ cells share an almost same thickness (Figure 6e), the dramatically higher interfacial R_{ct} in ex situ cells should originate from its poor-contacted and unstable interface.

Above results confirm that the integrated electrolyte-electrode interface with excellent compatibility and stability could induce lower interfacial impedance, uniform interfacial ion flux and homogeneous Zn deposition, supporting the dramatically improved electrochemical performance. At last, the outstanding performance of the *in-situ*-integrated solid-state Zn metal batteries demonstrated in this study is highlighted by a comparison with previous studies based on other polymer or composite electrolytes (Table S3). The MOF-Fc@PM electrolyte stands out with the high ionic conductivity of 1.52×10^{-3} S cm⁻² and excellent capacity output (123.9 mAh g⁻¹ after 2000 cycles) among all-solid-state ZMBs. As demonstrated, the *in-situ* polymerizable MOF-Fc@PM electrolyte with its record-high ionic conductivity, high tz_{n2+} , and superior interfacial stability can spur the development of all-solid-state rechargeable batteries.

Conclusions

In summary, we report a single-Zn²⁺ conducting MOF-Fc@PM electrolyte using a missing-linker MOF-Fc incorporated PEGDA-PAM copolymer matrix. The fundamental impacts of MOF-Fc fillers on anchoring OTF⁻ anions, reducing the crystallinity degree of polymer matrix, and facilitating the dissociation and migration of Zn²⁺ ions are elucidated, thereby addressing the inherent limitations of Zn²⁺ ion transport in SPEs. The strategic coordination between Zn²⁺ ions and PEGDA and PAM chains establishes a fast Zn²⁺ diffusion channel characterized by low migration energy barriers. As a result, the MOF-Fc@PM developed in this study presented mS cm⁻¹ levels of room temperature ionic conductivity and low Zn deposition overpotentials in all-solid-state conditions. Applications of *in-situ*

polymerization for MOF-Fc@PM electrolytes in Zn//Zn symmetric cells and Zn//VO₂ full cells demonstrate the formation of integrated electrolyte-electrolyte interfaces with excellent compatibility and stability, thus addressing the persistent issue of inadequate bulk and interfacial ion transport in solid-state ZMBs. The *in-situ*-integrated Zn//VO₂ cells deliver an extremely low capacity fading of 0.012 % per cycle over 2000 cycles, surpassing other liquid-free solid-state ZMBs. This work provides fresh insights into the design of high-performance all-solid-state ZMBs.

Methods

Preparation of MOF: 0.543 g (3 mmol) 2-aminoterephthalic acid (*Aladdin*, 99%) and 0.713 g (3 mmol) cobalt chloride hexahydrate (CoCl₂·6H₂O, *Aladdin*, AR) were dissolved in 15 mL N, N-dimethylformamide (DMF), respectively. The solutions were then slowly mixed in a 100 mL Teflon-lined stainless-steel autoclave, which is subsequently heated at 100 °C for 15 h. The solid products were obtained by flushing with DMF, deionized water, and methanol and being dried at 60 °C for 12 h in an oven.

Preparation of MOF-Fc: 0.543 g (3 mmol) 2-aminoterephthalic acid (*Aladdin*, 99%) and 0.115 g (0.5 mmol) ferrocenecarboxylic acid (Fc, *Macklin*, 98%) were dissolved in 15 mL DMF. Then, the solution was slowly mixed with 15 mL CoCl₂·6H₂O (0.713 mg, 3 mmol) DMF solution in a 100 mL Teflon-lined stainless-steel autoclave. Subsequently, the autoclave was heated at 100 °C for 15 h. The resulting products were obtained by washing the product with DMF, deionized water, and methanol three times and being dried at 60 °C for 12 h. The atomic contents of Co and Fe were measured by ICP-MS to determine the ratio of 2-aminoterephthalic acid and Fc in MOF-Fc.

Preparation of solid-state polymer electrolytes: Firstly, the as-prepared MOF powders (0.3 g) were mixed with 0.3 mL methacryloyl chloride (*Aladdin*, 95%) in 10.0 mL CH₂Cl₂, and then sealed in a vial and stored at room temperature for 100 h. The resulting solid was washed several times with CH₂Cl₂ and then dried under vacuum at 60 °C for 12 h to obtain the postmodified MOFs. Secondly, 1.2 g

poly(ethylene glycol) diacrylate (PEGDA, *Aladdin*, Mw~1000) and 0.3 g acrylamide (AM, *Aladdin*, 99%) were dissolved in CH₂Cl₂ (2 mL). 0.3 g postmodified MOF (MOF or MOF-Fc) powders, 5 mg 2,2'-Azobis(2-methylpropionitrile) (AIBN, *Aladdin*, 98%), and 0.2 g Zn(OTF)₂ (*Macklin*, 99%) were dispersed into 2 mL ethanol. These two solutions were mixed and ultrasonicated for 1 hour. The precursor solution was poured into a square PTFE mold and then heated for 3 hours at 50 °C to get the solidified electrolyte films. Finally, the films were heated at 80 °C for 2 hours to completely remove the solvent. The PEGDA and PEGDA-PAM-based electrolytes were synthesized by a similar method without adding MOF fillers.

*Preparation of VO*₂ *cathode*: VO₂ cathode materials were synthesized by a simple hydrothermal method as reported in the literature. Typically, 4 mmol V₂O₅ (*Aladdin*, 99%), 9.6 mmol H₂C₂O₄·2H₂O (*Aladdin*, 98%), and 3.4 mmol PEG-4000 (*Aladdin*, 3500-4000) were added into 66 mL DI water. After magnetic stirring at 40 °C for 24 h, a homogeneous solution was obtained. Then, the solution was transferred into a 100 mL Teflon-lined stainless-steel autoclave to be heated at 180 °C for 24 h. Afterward, the reactors were cooled down to room temperature naturally. The VO₂ products were collected by washing with deionized water and pure alcohol several times. They were finally dried at 70 °C for 24 h before using.

To prepare the VO₂ cathode, the active materials, PVDF, and acetylene black (Super-P) were mixed at a weight ratio of 70:15:15 in N-Methylpyrrolidone (*Aladdin*, 99.99%) to form a homogeneous slurry. The homogeneous slurry was cast onto a carbon paper substrate and dried at 60 °C for 12 h.

Materials characterizations: The crystal structure of the as-synthesized materials was studied on a Rigaku Ultima IV XRD equipped with a Cu Kα source (λ=1.5405 Å). The morphologies, microstructure and elemental compositions were investigated by a field emission SEM (Tescan MAIA3). Chemical compositions of the samples were analyzed by high-resolution XPS (ThermoFischer, ESCALLAB Xi+). The high-resolution iDPC-STEM images were captured under a Cs-corrected STEM (Thermo ScientificTM Spectra 300 S/TEM) operated at 300 kV. All the datasets

were acquired using a probe at 300 keV beam energy and 29.9 mrad probe-forming semi-angle. The electron-beam current was reduced < 1 pA by unfiltered monochromator. The dwell time was 2 μs and the electron dose was < 210 e⁻/Å². FTIR characterization was performed on Thermo Scientific iN10. Raman spectra were performed on a Horiba LabRAM HR Evolution Raman spectrometer with a 633 nm laser as an excitation source. Tensile strength was tested by a microcomputer-controlled electronic universal testing machine (Shimadzu AGS-X-50N). DSC was performed by a Netzsch DSC 200 F3 synchronous thermal analyzer with a heating rate of 10 °C min⁻¹. TGA was performed by HITACHI STA200 thermal analyzer. The chemical content was estimated by the ICP Optical emission spectrometer Agilent 720ES(OES). The Co XANES spectroscopy was performed by EasyXAFS300+ (Easy XAFS).

Electrochemical measurements: The in-situ Zn//Zn and Zn//VO₂ cells are constructed by uniformly coating the liquid electrolyte precursor in the middle of two electrodes, which is solidified after being heated at 50 °C for 2 hours. The ex-situ cell is constructed by sandwiching prefabricated solid electrolyte films into the middle of electrodes. The batteries are assembled in CR2032-type coin cell. Cyclic voltammetry (CV) curves, chromoamperograms (CAs), and electrochemical impedance spectroscopy (EIS) were tested on a CHI 760e electrochemical workstation (CHI760D, Chenhua, Shanghai). Galvanostatic charge/discharge cycling measurements were conducted on Neware CT-3008 battery testers. The electrochemical stability windows of electrolytes were tested using the carbon coated Al foil as working electrode.

The ionic conductivity of the as-prepared electrolytes was obtained through an alternating current (AC) impedance measurement of SS/electrolyte/SS cell over a frequency ranging from 1 MHz to 100 mHz with an amplitude of 5 mV at various temperatures from 25 to 65 °C. The ionic conductivity (σ) was calculated as Equation (1):

$$\sigma = \frac{L}{RA} \tag{1}$$

where L, A, and R represent the thickness, the area of electrolyte between the two stainless steels, and

the bulk resistance of the electrolyte, respectively.

The activation energy (E_a) was calculated by the Arrhenius Equation:

$$\sigma(T) = Aexp\left(-\frac{E_a}{RT}\right) \tag{2}$$

where A is the pre-exponential factor, E_a is the activation energy of activated ion-hopping conduction process, and T is the absolute temperature.

The impedance of the Zn//Zn symmetric cell was measured before and after polarization with a DC voltage pulse (10 mV) with a Gamry Interface 1000 Potentiostat. The Zn ion transference numbers, t_{Zn2+} , was calculated by Equation (3):

$$t_{\rm Zn2+} = I_{\rm S} (\Delta V - I_0 R_0) / I_0 (\Delta V - I_{\rm S} R_{\rm S})$$
 (3)

where I_S and I_θ are the steady-state and initial currents, respectively, and R_S and R_θ are the corresponding steady-state and initial resistances.

DFT calculations: The DFT calculations are implemented using Vienna ab initio Simulation Package (VASP),^{53,54} and Gaussian 16 package.⁵⁵ For the simulations of MOF-based models, periodic boundary conditions are adopted and 1\times2\times2 supercells are created to weaken the instability induced by the vacancy in neighbor cells. The projector-augmented wave (PAW) is used to describe the interactions between ions and electrons. The widely used exchange-correlation functional, PBE, is adopted with the correction of the DFT-D3 method. The empirical Hubbard U parameter for the 3d electrons of Co is set to 4 eV according to a previous report.¹⁹ The criterion of convergence in geometric optimization is 0.02 eV/Angstrom and 1\times10⁻⁵ eV in single-point energy calculations. Interactions of Zn²⁺ with PAM and PEGDA polymers are simulated using the Gaussian 16 package at the B3LYP/6-311G level of theory in geometric optimizations. The energy calculations of Zn-polymer systems adopt the M06-2X functional and def2-TZVP basis set.

Supporting Information

Additional figures include the SEM images, crystal structures calculated by DFT simulation, iDPC-STEM images and derived strain mapping images, general XPS survey, Co 2p XPS, O 1s XPS, the valence band spectra, EPR spectra, Co K-edge of XANES spectra, Co K-edge of k3χ(k) oscillation curves, Fourier-transform Co K-edge EXAFS spectra, the wavelet transform contour plots, Barret-Joyner-Halenda (BJH) pore size distribution spectra, DFT calculated Zn²⁺ adsorption configurations of MOF and MOF-Fc, FTIR spectra of MOF and MOF-Fc before and after being modified by methacryloyl chloride, SEM images, TGA curves and Tensile stress-strain curves of the electrolyte films, Co K-edge XANES spectra of MOF and MOF-Fc before and after immersion in Zn(OTF)₂ solution, current-time plots and the corresponding EIS spectra of electrolytes, capacity of the Zn//Cu asymmetric cell, SEM images, XRD pattern, TEM images of VO₂, electrochemical performance for the *in situ* and *ex situ* cells.

Author contributions

Xiaobin Hui, Zhen Zhan, and Zeyu Zhang contributed equally to this work.

X.H. and Z.X. designed the project. X.H., P.J., and J.Y. performed the syntheses and electrochemical tests. Z.Z. and S.C. carried out the iDPC-STEM characterizations. Z.Y. and Z.D. performed the DFT calculations. J.W. tested the XANES and EXAFS. X.H., Z.Y.Z., and Z.X. prepared the manuscript. X.H., Z.X., Y.W., and S.C. proposed the mechanism investigation and wrote the manuscript. All authors participated in the discussion of experimental and calculation results.

Conflicts of Interest

The authors declare no conflict of interest

Data availability

Full data supporting the findings of this study are available within the article and its Supplementary Information, as well as from the corresponding author upon reasonable request.

Acknowledgements

The work described in this paper was supported by funding supports from the Research Institute of Advanced Manufacturing (RIAM) and the State Key Laboratory of Ultra-precision Machining Technology (SKL-UPMT) of the Hong Kong Polytechnic University (project No. 1-CD4M, 1-BBR0) and the PolyU Distinguished Postdoctoral Fellowship Scheme (project No. 1-YWD8), Department of Science and Technology of Guangdong Province (Project No. 2022A1515010206). S.C. acknowledges the support of the startup grant from the Department of Applied Physics, the Hong Kong Polytechnic University (1-BDCM), and the Hong Kong Research Grants Council General Research Fund (No. 15306122).

References

- 1. Ma, L.; Schroeder, M. A.; Borodin, O.; Pollard, T. P.; Ding, M. S.; Wang, C.; Xu, K. Realizing high zinc reversibility in rechargeable batteries. *Nature Energy* **2020**, *5* (10), 743-749.
- 2. Cao, L.; Li, D.; Pollard, T.; Deng, T.; Zhang, B.; Yang, C.; Chen, L.; Vatamanu, J.; Hu, E.; Hourwitz, M. J. Fluorinated interphase enables reversible aqueous zinc battery chemistries. *Nature Nanotechnology* **2021**, *16* (8), 902-910.
- 3. Zhang, T.; Tang, Y.; Guo, S.; Cao, X.; Pan, A.; Fang, G.; Zhou, J.; Liang, S. Fundamentals and perspectives in developing zinc-ion battery electrolytes: a comprehensive review. *Energy & Environmental Science* **2020**, *13* (12), 4625-4665.
- 4. Jia, X.; Liu, C.; Neale, Z. G.; Yang, J.; Cao, G. Active materials for aqueous zinc ion batteries: synthesis, crystal structure, morphology, and electrochemistry. *Chemical Reviews* **2020**, *120* (15), 7795-7866.
- 5. Zou, Z.; Li, Y.; Lu, Z.; Wang, D.; Cui, Y.; Guo, B.; Li, Y.; Liang, X.; Feng, J.; Li, H. Mobile ions in

- composite solids. *Chemical reviews* **2020**, *120* (9), 4169-4221.
- 6. Fang, G.; Zhou, J.; Pan, A.; Liang, S. Recent advances in aqueous zinc-ion batteries. *ACS Energy Letters* **2018**, *3* (10), 2480-2501.
- 7. Ge, H.; Xie, X.; Xie, X.; Zhang, B.; Li, S.; Liang, S.; Lu, B.; Zhou, J. Critical challenges and solutions: quasi-solid-state electrolytes for zinc-based batteries. *Energy & Environmental Science* **2024**, *17* (1), 327-336.
- 8. Ma, L.; Chen, S.; Li, N.; Liu, Z.; Tang, Z.; Zapien, J. A.; Chen, S.; Fan, J.; Zhi, C. Hydrogen-free and dendrite-free all-solid-state Zn-ion batteries. *Advanced Materials* **2020**, *32* (14), 1908121.
- 9. Hansen, E. J.; Liu, J. Materials and structure design for solid-state zinc-ion batteries: A mini-review. *Frontiers in Energy Research* **2021**, *8*, 616665.
- 10. Chen, Z.; Li, X.; Wang, D.; Yang, Q.; Ma, L.; Huang, Z.; Liang, G.; Chen, A.; Guo, Y.; Dong, B. Grafted MXene/polymer electrolyte for high performance solid zinc batteries with enhanced shelf life at low/high temperatures. *Energy & Environmental Science* **2021**, *14* (6), 3492-3501.
- 11. Yang, H.; Liu, B.; Bright, J.; Kasani, S.; Yang, J.; Zhang, X.; Wu, N. A single-ion conducting UIO-66 metal-organic framework electrolyte for all-solid-state lithium batteries. *ACS Applied Energy Materials* **2020**, *3* (4), 4007-4013.
- 12. Sand, H. J. III. On the concentration at the electrodes in a solution, with special reference to the liberation of hydrogen by electrolysis of a mixture of copper sulphate and sulphuric acid. *The London, Edinburgh, and Dublin Philosophical Magazine and Journal of Science* **1901**, *1* (1), 45-79.
- 13. Wang, Z.; Hu, J.; Han, L.; Wang, Z.; Wang, H.; Zhao, Q.; Liu, J.; Pan, F. A MOF-based single-ion Zn²⁺ solid electrolyte leading to dendrite-free rechargeable Zn batteries. *Nano energy* **2019**, *56*, 92-99.
- 14. Chen, Z.; Wang, T.; Hou, Y.; Wang, Y.; Huang, Z.; Cui, H.; Fan, J.; Pei, Z.; Zhi, C. Polymeric Single-Ion Conductors with Enhanced Side-Chain Motion for High-Performance Solid Zinc-Ion Batteries. *Advanced Materials* **2022**, *34* (50), 2207682.
- 15. Yao, L.; Hou, C.; Liu, M.; Chen, H.; Zhao, Q.; Zhao, Y.; Wang, Y.; Liu, L.; Yin, Z. W.; Qiu, J. Ultra-

- Stable Zn Anode Enabled by Fiber-Directed Ion Migration Using Mass-Producible Separator. *Advanced Functional Materials* **2023**, *33* (5), 2209301.
- 16. Xia, H.; Xu, G.; Cao, X.; Miao, C.; Zhang, H.; Chen, P.; Zhou, Y.; Zhang, W.; Sun, Z. Single-Ion Conducting Hydrogel Electrolytes based on Slide-ring Pseudo-polyrotaxane for Ultra-long Cycling Flexible Zinc-Ion Batteries. *Advanced Materials* **2023**, *35* (36), 2301996.
- 17. Lv, Y.; Xiao, Y.; Ma, L.; Zhi, C.; Chen, S. Recent advances in electrolytes for "beyond aqueous" zinc-ion batteries. *Advanced Materials* **2022**, *34* (4), 2106409.
- 18. Qiu, T.; Wang, T.; Tang, W.; Li, Y.; Li, Y.; Lang, X.; Jiang, Q.; Tan, H. Rapidly Synthesized Single-Ion Conductive Hydrogel Electrolyte for High-Performance Quasi-Solid-State Zinc-ion Batteries. *Angewandte Chemie* **2023**, *135* (45), e202312020.
- 19. Xue, Z.; Liu, K.; Liu, Q.; Li, Y.; Li, M.; Su, C.-Y.; Ogiwara, N.; Kobayashi, H.; Kitagawa, H.; Liu, M. Missing-linker metal-organic frameworks for oxygen evolution reaction. *Nature communications* **2019**, *10* (1), 5048.
- 20. Ding, J.; Guo, D.; Wang, N.; Wang, H. F.; Yang, X.; Shen, K.; Chen, L.; Li, Y. Defect Engineered Metal-Organic Framework with Accelerated Structural Transformation for Efficient Oxygen Evolution Reaction. *Angewandte Chemie International Edition* **2023**, *62* (43), e202311909.
- 21. Shen, B.; Chen, X.; Shen, K.; Xiong, H.; Wei, F. Imaging the node-linker coordination in the bulk and local structures of metal-organic frameworks. *Nature Communications* **2020**, *11* (1), 2692.
- 22. Zhan, Z.; Liu, Y.; Wang, W.; Du, G.; Cai, S.; Wang, P. Atomic-level imaging of beam-sensitive COFs and MOFs by low-dose electron microscopy. *Nanoscale Horizons* **2024**, doi: 10.1039/D3NH00494E.
- 23. Sun, D.; Wong, L. W.; Wong, H. Y.; Lai, K. H.; Ye, L.; Xv, X.; Ly, T. H.; Deng, Q.; Zhao, J. Direct Visualization of Atomic Structure in Multivariate Metal-Organic Frameworks (MOFs) for Guiding Electrocatalysts Design. *Angewandte Chemie* **2023**, *135* (4), e202216008.

- 24. Cabral, M. J.; Chen, Z.; Liao, X. Scanning transmission electron microscopy for advanced characterization of ferroic materials. *Microstructures* **2023**, *3*, 2023040.
- 25. Cai, S.; Dai, J.; Shao, Z.; Rothmann, M. U.; Jia, Y.; Gao, C.; Hao, M.; Pang, S.; Wang, P.; Lau, S. P. Atomically resolved electrically active intragrain interfaces in perovskite semiconductors. *Journal of the American Chemical Society* **2022**, *144* (4), 1910-1920.
- 26. Dahéron, L.; Dedryvère, R.; Martinez, H.; Ménétrier, M.; Denage, C.; Delmas, C.; Gonbeau, D. Electron transfer mechanisms upon lithium deintercalation from LiCoO₂ to CoO₂ investigated by XPS. *Chemistry of Materials* **2008**, *20* (2), 583-590.
- 27. Ravel, B.; Newville, M. ATHENA, ARTEMIS, HEPHAESTUS: data analysis for X-ray absorption spectroscopy using IFEFFIT. *Journal of synchrotron radiation* **2005**, *12* (4), 537-541.
- 28. Tang, W.; Tang, S.; Zhang, C.; Ma, Q.; Xiang, Q.; Yang, Y. W.; Luo, J. Simultaneously enhancing the thermal stability, mechanical modulus, and electrochemical performance of solid polymer electrolytes by incorporating 2D sheets. *Advanced Energy Materials* **2018**, *8* (24), 1800866.
- 29. Diederichsen, K. M.; Buss, H. G.; McCloskey, B. D. The compensation effect in the Vogel-Tammann-Fulcher (VTF) equation for polymer-based electrolytes. *Macromolecules* **2017**, *50* (10), 3831-3840.
- 30. Nandiyanto, A. B. D.; Oktiani, R.; Ragadhita, R. How to read and interpret FTIR spectroscope of organic material. *Indonesian Journal of Science and Technology* **2019**, *4* (1), 97-118.
- 31. Wang, H.; Wang, Q.; Cao, X.; He, Y.; Wu, K.; Yang, J.; Zhou, H.; Liu, W.; Sun, X. Thiol-branched solid polymer electrolyte featuring high strength, toughness, and lithium ionic conductivity for lithium-metal batteries. *Advanced Materials* **2020**, *32* (37), 2001259.
- 32. Lin, P.; Cong, J.; Li, J.; Zhang, M.; Lai, P.; Zeng, J.; Yang, Y.; Zhao, J. Achieving ultra-long lifespan Zn metal anodes by manipulating desolvation effect and Zn deposition orientation in a multiple cross-linked hydrogel electrolyte. *Energy Storage Materials* **2022**, *49*, 172-180.
- 33. Cao, X.; Xu, W.; Zheng, D.; Wang, F.; Wang, Y.; Shi, X.; Lu, X. Weak Solvation Effect Induced

- Optimal Interfacial Chemistry Enables Highly Durable Zn Anodes for Aqueous Zn-Ion Batteries. Angewandte Chemie International Edition **2024**, 63 (6), e202317302.
- 34. Ming, F.; Zhu, Y.; Huang, G.; Emwas, A.-H.; Liang, H.; Cui, Y.; Alshareef, H. N. Co-solvent electrolyte engineering for stable anode-free zinc metal batteries. *Journal of the American Chemical Society* **2022**, *144* (16), 7160-7170.
- 35. Feng, X.; Li, P.; Yin, J.; Gan, Z.; Gao, Y.; Li, M.; Cheng, Y.; Xu, X.; Su, Y.; Ding, S. Enabling highly reversible Zn anode by multifunctional synergistic effects of hybrid solute additives. *ACS Energy Letters* **2023**, *8* (2), 1192-1200.
- 36. Kim, M.; Lee, J.; Kim, Y.; Park, Y.; Kim, H.; Choi, J. W. Surface Overpotential as a Key Metric for the Discharge-Charge Reversibility of Aqueous Zinc-Ion Batteries. *Journal of the American Chemical Society* **2023**, *145* (29), 15776-15787.
- 37. Dong, P.; Zhang, X.; Hiscox, W.; Liu, J.; Zamora, J.; Li, X.; Su, M.; Zhang, Q.; Guo, X.; McCloy,
- J. Toward High-Performance Metal-Organic-Framework-Based Quasi-Solid-State Electrolytes: Tunable Structures and Electrochemical Properties. *Advanced Materials* **2023**, *35* (32), 2211841.
- 38. Wang, D.; Lv, D.; Peng, H.; Wang, C.; Liu, H.; Yang, J.; Qian, Y. Solvation Modulation Enhances Anion-Derived Solid Electrolyte Interphase for Deep Cycling of Aqueous Zinc Metal Batteries. *Angewandte Chemie International Edition* **2023**, *62* (38), e202310290.
- 39. Wang, Y.; Liang, B.; Zhu, J.; Li, G.; Li, Q.; Ye, R.; Fan, J.; Zhi, C. Manipulating Electric Double Layer Adsorption for Stable Solid-Electrolyte Interphase in 2.3 Ah Zn-Pouch Cells. *Angewandte Chemie* **2023**, *135* (23), e202302583.
- 40. Li, C.; Zhu, X.; Wang, D.; Yang, S.; Zhang, R.; Li, P.; Fan, J.; Li, H.; Zhi, C. Fine Tuning Water States in Hydrogels for High Voltage Aqueous Batteries. *ACS nano* **2024**, *18* (4), 3101-3114.
- 41. Xu, G.; Zhang, Y.; Jiang, M.; Li, J.; Sun, H.; Li, J.; Lu, T.; Wang, C.; Yang, G.; Pan, L. A machine learning-assisted study on organic solvents in electrolytes for expanding the electrochemical stable window of zinc-ion batteries. *Chemical Engineering Journal* **2023**, *476*, 146676.

- 42. Zhang, H.; Liu, X.; Li, H.; Hasa, I.; Passerini, S. Challenges and strategies for high-energy aqueous electrolyte rechargeable batteries. *Angewandte Chemie International Edition* **2021**, *60* (2), 598-616.
- 43. Yang, X.; Liu, J.; Pei, N.; Chen, Z.; Li, R.; Fu, L.; Zhang, P.; Zhao, J. The critical role of fillers in composite polymer electrolytes for lithium battery. *Nano-Micro Letters* **2023**, *15* (1), 74.
- 44. Huo, S.; Sheng, L.; Xue, W.; Wang, L.; Xu, H.; Zhang, H.; He, X. Challenges of polymer electrolyte with wide electrochemical window for high energy solid-state lithium batteries. *InfoMat* **2023**, *5* (3), e12394.
- 45. Duan, S.; Qian, L.; Zheng, Y.; Zhu, Y.; Liu, X.; Dong, L.; Yan, W.; Zhang, J. Mechanisms of the Accelerated Li⁺ Conduction in MOF-based Solid-State Polymer Electrolytes for All-Solid-State Lithium Metal Batteries. *Advanced Materials* **2024**, *36* (32), 2314120.
- 46. Park, S. S.; Tulchinsky, Y.; Dincă, M. Single-ion Li⁺, Na⁺, and Mg²⁺ solid electrolytes supported by a mesoporous anionic Cu-azolate metal-organic framework. *Journal of the American Chemical Society* **2017**, *139* (38), 13260-13263.
- 47. Zhao, Z.; Nian, B.; Lei, Y.; Wang, Y.; Shi, L.; Yin, J.; Mohammed, O. F.; Alshareef, H. N. A Novel Plastic-Crystal Electrolyte with Fast Ion-Transport Channels for Solid Zinc-Ion Batteries. *Advanced Energy Materials* **2023**, *13* (21), 2300063.
- 48. Qiu, B.; Liang, K.; Huang, W.; Zhang, G.; He, C.; Zhang, P.; Mi, H. Crystal-Facet Manipulation and Interface Regulation *via* TMP-Modulated Solid Polymer Electrolytes toward High-Performance Zn Metal Batteries. *Advanced Energy Materials* **2023**, *13* (32), 2301193.
- 49. Wang, J.; Zhao, Z.; Lu, G.; Zhang, Y.; Kong, Q.; Zhao, J.; Cui, G. Room-temperature fast zinc-ion conduction in molecule-flexible solids. *Materials Today Energy* **2021**, *20*, 100630.
- 50. Wu, P.; Xu, L.; Xiao, X.; Ye, X.; Meng, Y.; Liu, S. An Industrially Applicable Passivation Strategy for Significantly Improving Cyclability of Zinc Metal Anodes in Aqueous Batteries. *Advanced Materials* **2024**, *36* (2), 2306601.
- 51. Tian, C.; Wang, J.; Sun, R.; Ali, T.; Wang, H.; Xie, B. B.; Zhong, Y.; Hu, Y. Improved Interfacial

- Ion Migration and Deposition through the Chain-Liquid Synergistic Effect by a Carboxylated Hydrogel Electrolyte for Stable Zinc Metal Anodes. *Angewandte Chemie International Edition* **2023**, 62 (42), e202310970.
- 52. Chen, L.; Ruan, Y.; Zhang, G.; Wei, Q.; Jiang, Y.; Xiong, T.; He, P.; Yang, W.; Yan, M.; An, Q. Ultrastable and high-performance Zn/VO₂ battery based on a reversible single-phase reaction. *Chemistry of Materials* **2019**, *31* (3), 699-706.
- 53. Kresse, G.; Hafner, J. Ab initio molecular-dynamics simulation of the liquid-metal–amorphous-semiconductor transition in germanium. *Physical Review B* **1994**, *49* (20), 14251.
- 54. Kresse, G.; Furthmüller, J. Efficiency of ab-initio total energy calculations for metals and semiconductors using a plane-wave basis set. *Computational materials science* **1996**, *6* (1), 15-50.
- 55. Frisch, M.; Trucks, G.; Schlegel, H. B.; Scuseria, G.; Robb, M.; Cheeseman, J.; Scalmani, G.; Barone, V.; Petersson, G.; Nakatsuji, H. Gaussian 16, Gaussian. *Inc., Wallingford CT* **2016**, GaussView 5.0. Wallingford, E.U.A.

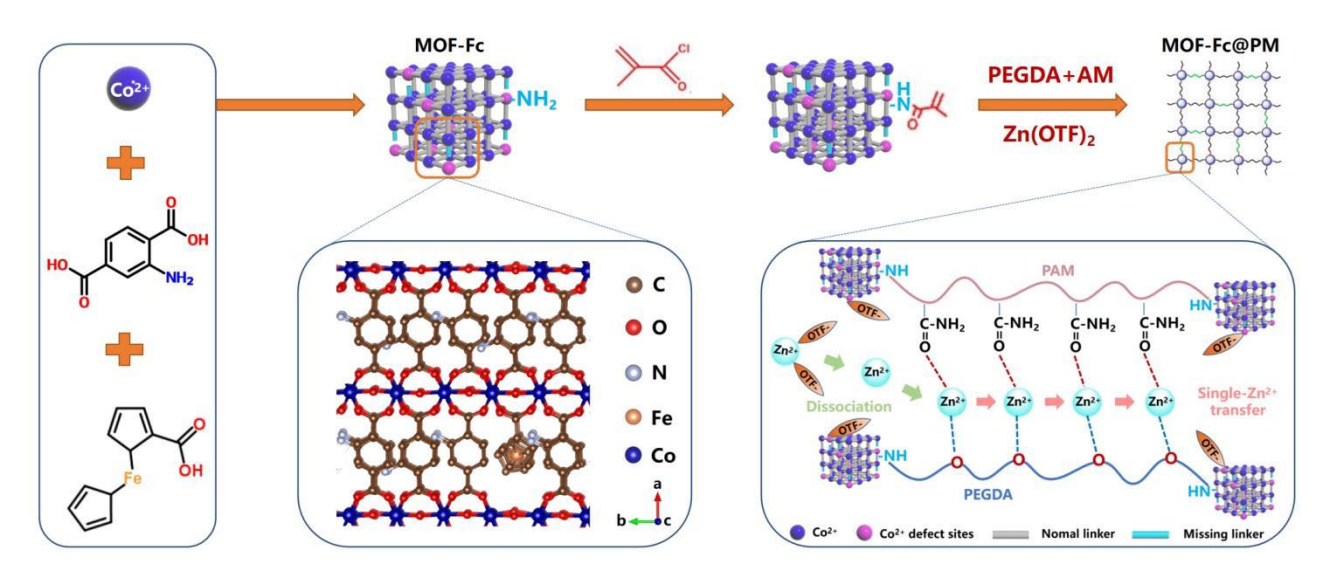


Figure 1. Schematic illustration of the fabrication process and the single Zn^{2+} conducting mechanism for the MOF-Fc@PM electrolyte.

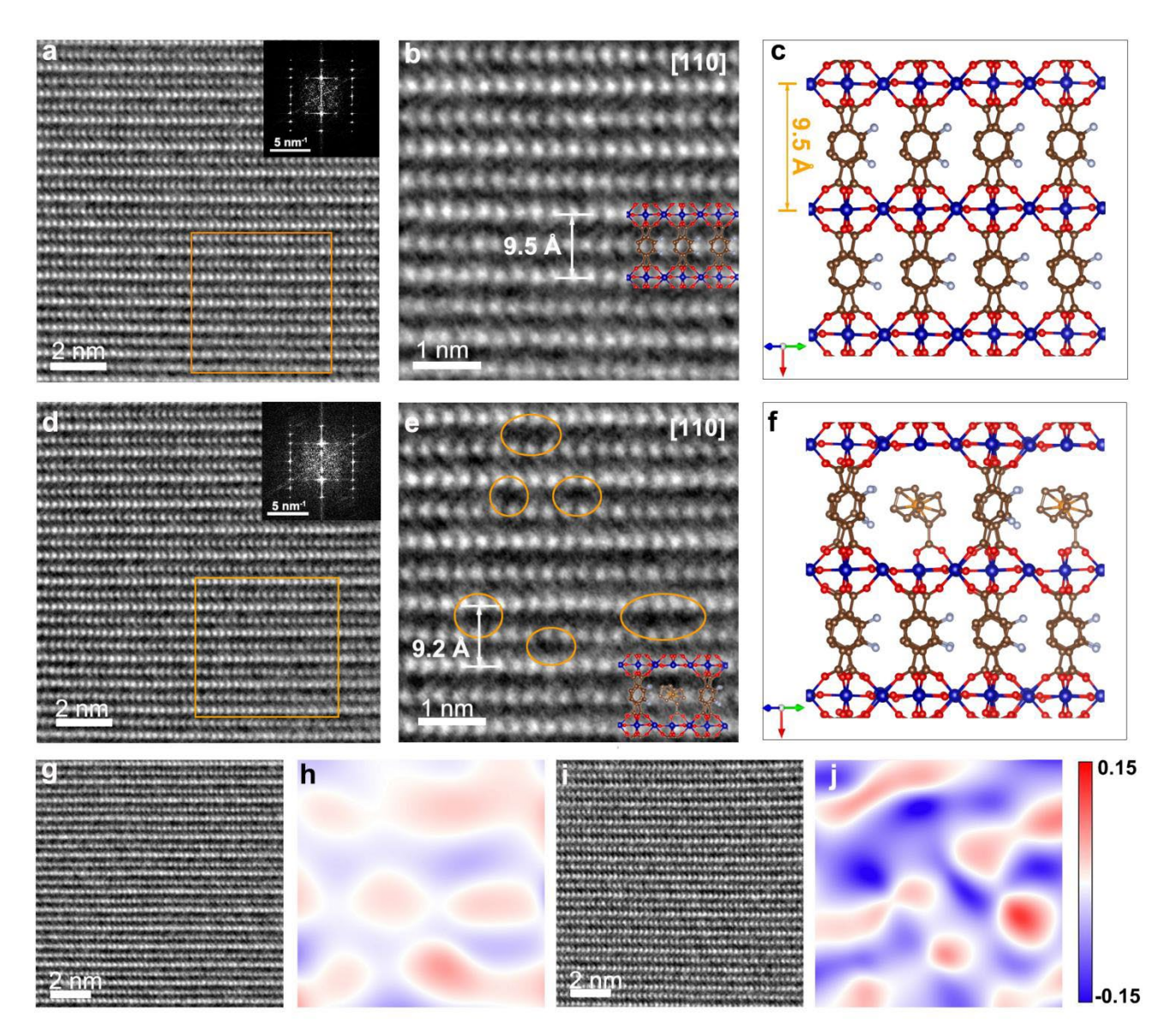


Figure 2. Morphology and structural model of missing-linker MOFs: a, b the iDPC-STEM images (the insert is the corresponding fast Fourier transform image) and c the corresponding structural model of MOF. d, e the iDPC-STEM images (the insert is the corresponding fast Fourier transform image) and f the corresponding structural model of MOF-Fc. The iDPC-STEM and derived strain mapping (*E*_{yy} direction) images of g, h MOF and i, j MOF-Fc.

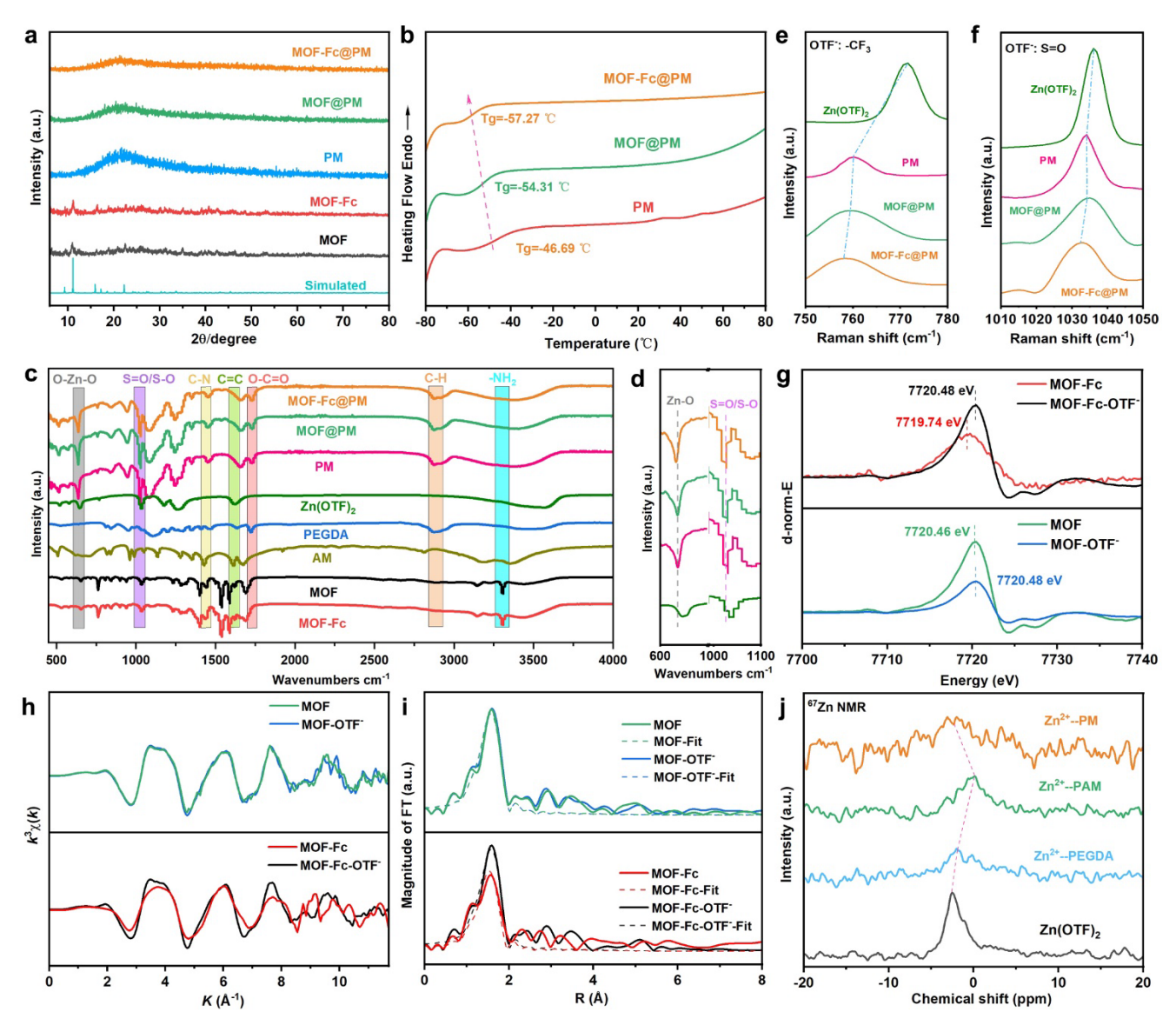


Figure 3. Chemical structures of missing-linker MOF regulated solid-state polymer electrolyte: **a** XRD patterns, **b** DSC curves, **c**, **d** FTIR spectra, and **e**, **f** Raman spectra of the MOF-Fc@PM electrolytes and controlling samples. **g** Co K-edge energy (E₀) of XANES spectra, **h** Co K-edge EXAFS of oscillations, and **i** Fourier transformed EXAFS spectra for MOF and MOF-Fc before and after being immersed in Zn(OTF)₂ solution (designated as MOF-OTF⁻ and MOF-Fc-OTF⁻). **j** ⁶⁷Zn NMR spectra of Zn(OTF)₂ solutions containing PAM, PEGDA, or PEGDA-PAM polymer additives.

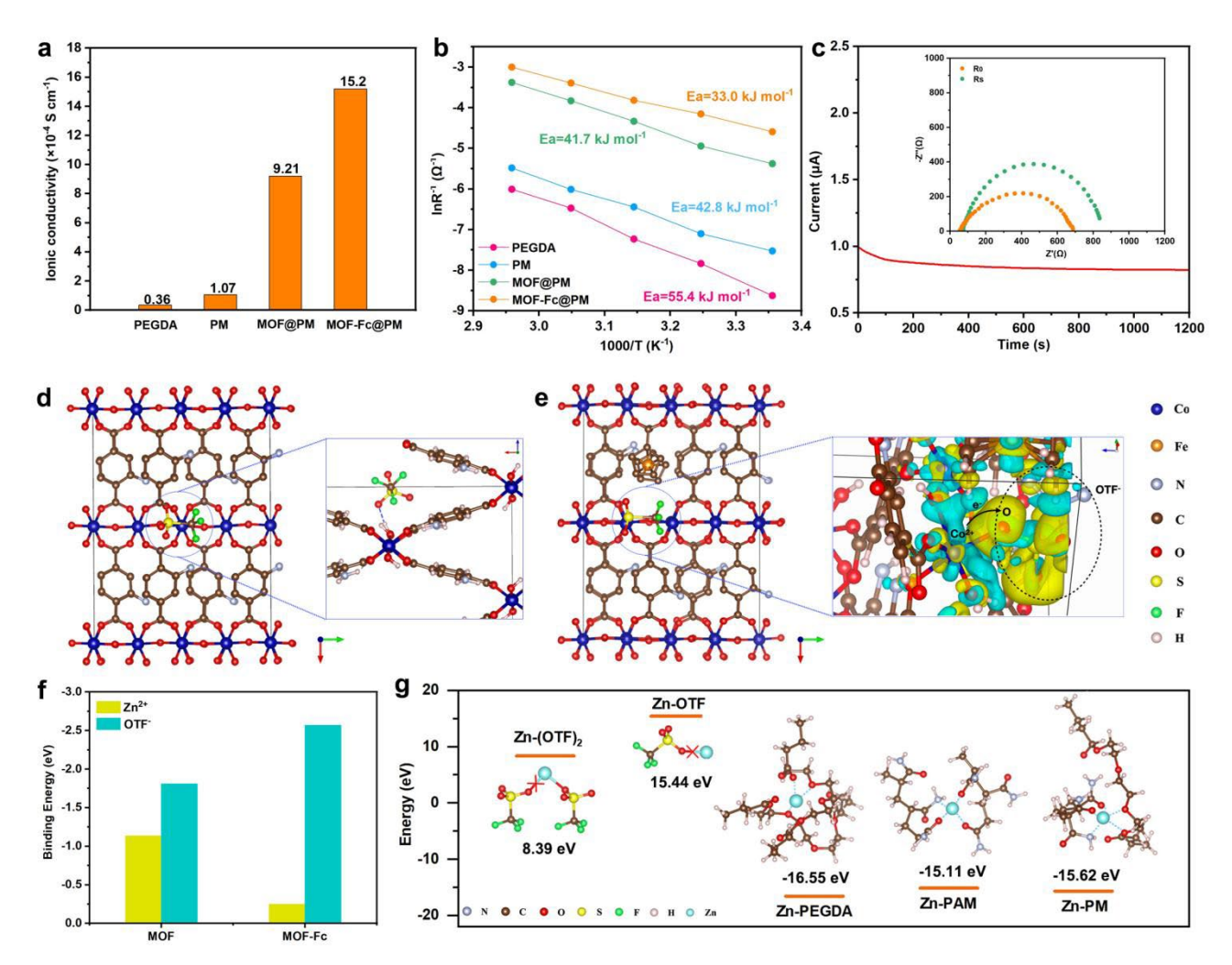


Figure 4. Zn²⁺ conduction properties and working mechanisms of MOF-Fc@PM electrolyte: a Ionic conductivity at room temperature and b Arrhenius plots of the PAGDA, PM, MOF@PM and MOF-Fc@PM electrolytes. c Current-time plot and EIS spectra of MOF-Fc@PM electrolyte for tzn2+ measurements. The DFT calculated OTF⁻ adsorption configurations for d MOF (the enlarged figure shows the adsorption of OTF⁻ on MOF through hydrogen bond) and e MOF-Fc (the enlarged figure shows the charge-density difference plots of MOF-Fc adsorbing OTF⁻ anion). f DFT calculated adsorption energies of Zn²⁺ and OTF⁻ for MOF and MOF-Fc. g The calculated dissociation energies of Zn-(OTF)₂ and Zn-OTF, and the solvation energies of PEGDA, PAM, and PM toward Zn²⁺ ions.

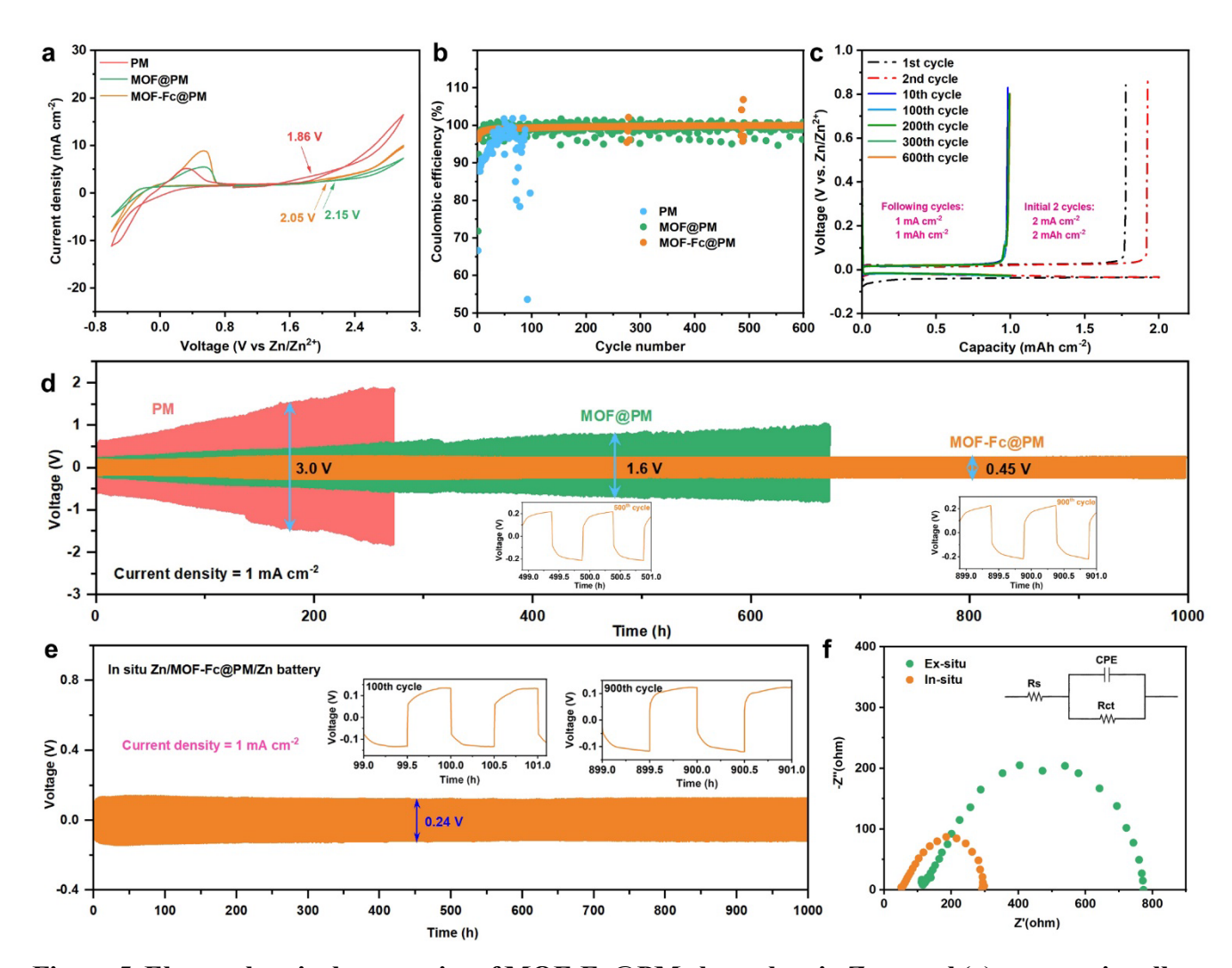


Figure 5. Electrochemical properties of MOF-Fc@PM electrolyte in Zn metal (a)symmetric cells:

a Electrochemical stability windows of PM, MOF@PM and MOF-Fc@PM electrolytes measured by CV curves in Zn//Al@C asymmetric cells. **b** Coulombic efficiencies of Zn deposition and **c** voltage profiles for the Zn//Cu asymmetric cells. **d** Zn plating/stripping profiles of Zn//Zn symmetrical cells with PM, MOF@PM, and MOF-Fc@PM electrolytes at a current density of 1 mA cm⁻² and a capacity of 0.5 mAh cm⁻². The inset is the voltage profiles at the 500th and 900th cycles. **e** Zn plating/stripping in *in-situ*-integrated Zn//Zn symmetric cells at 1 mA cm⁻². The inset is the voltage profiles at the 100th and 900th cycles. **f** Nyquist plots of the *in-situ* and *ex-situ* Zn//Zn cells before cycling.

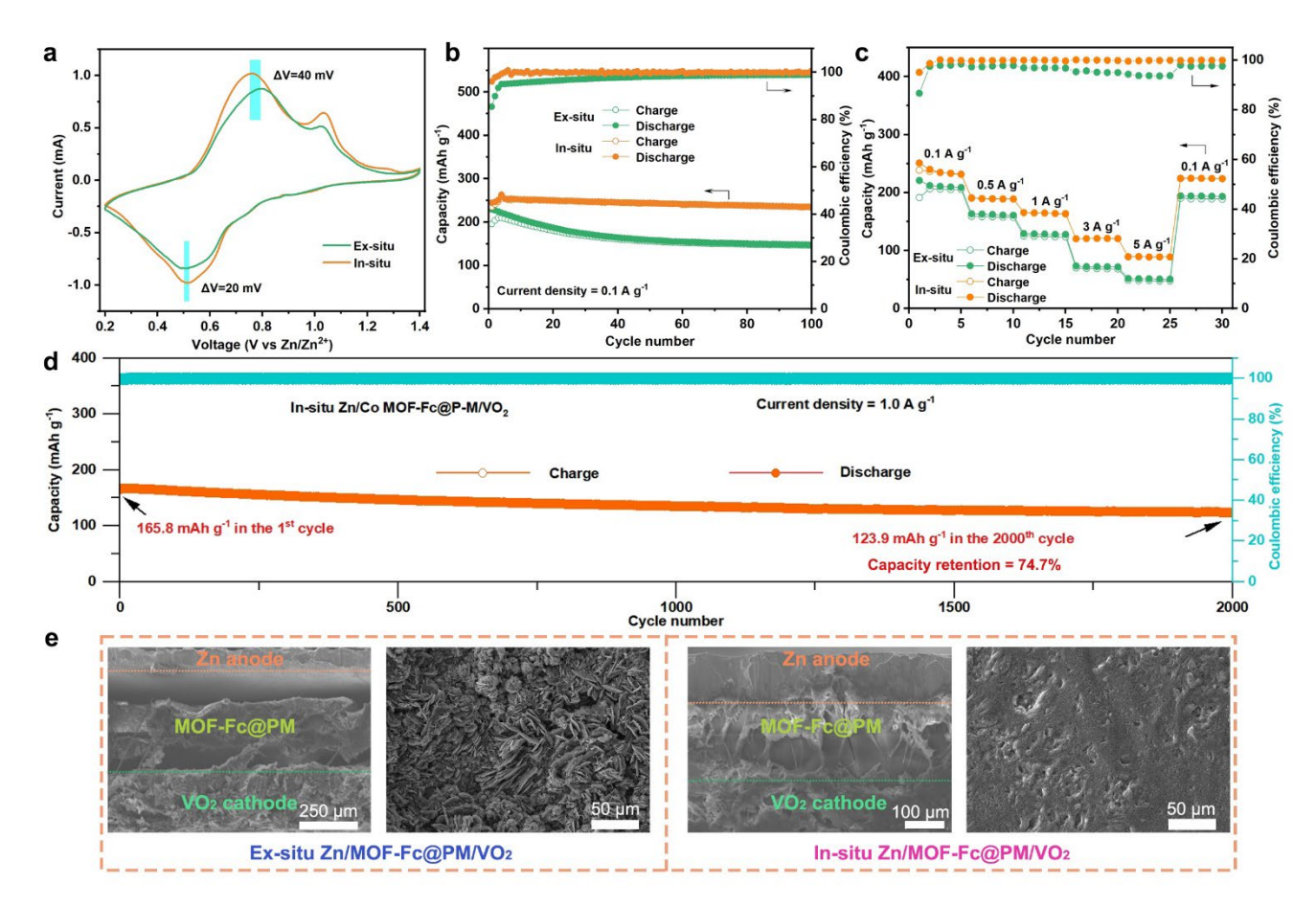


Figure 6. Electrochemical performance of solid-state Zn//VO₂ full cells: a CV curves at 0.1 mV s⁻¹, **b** Charge/discharge capacities and Coulombic efficiencies at 0.1 A g⁻¹ for 100 cycles, and **c** rate capability from 0.1 A g⁻¹ to 5 A g⁻¹ of the *in-situ* and *ex-situ* full cells. **d** Long-term cyclic capacities and Coulombic efficiencies of the *in-situ* full-cell. **e** Side-view SEM images of the *in-situ* (right) and *ex-situ* (left) full cells and the top-view SEM images of cycled Zn anodes in the corresponding full cells.

For Table of Contents Only

